Local, Explicit, and Charge-Conserving Electromagnetic Particle-In-Cell Algorithm on Unstructured Grids

Dong-Yeop Na, *Student Member, IEEE*, Haksu Moon, Yuri A. Omelchenko, and Fernando L. Teixeira, *Fellow, IEEE*

***Abstract*— We present a charge-conserving electromagnetic particle-in-cell (EM-PIC) algorithm on unstructured grids based on a finite element (FE) time-domain methodology with explicit field update, i.e., requiring no linear solver. The proposed explicit EM-PIC algorithm attains charge conservation from first principles by representing fields, currents, and charges by differential forms of various degrees, following the methodology put forth in reference [25]. The need for a linear solver is obviated by constructing a sparse approximate inverse (SPAI) for the FE system matrix, which also preserves the locality (sparsity) of the algorithm. We analyze in detail the residual error caused by SPAI on the motions of charged particles and beam trajectories and show that this error is several orders of magnitude smaller than the inherent error caused by the spatial and temporal discretizations.**

***Index Terms*— Charge conservation, finite elements (FEs), particle-in-cell, plasma, sparse approximated inverse.**

I. Introduction

In THE past few decades, electromagnetic particle-in-cell (EM-PIC) algorithms coupled to time-dependent Maxwell's equations [1]–[3] have been applied to a variety of problems involving charged particles and beam-wave interaction, including plasma-based accelerators [4]–[7], inertial confinement fusion [8], [9], and vacuum electronic devices [10]–[15]. Historically, EM-PIC algorithms have been mostly based upon regular grids and finite-difference approaches [16], [17] such as the celebrated Yee's finite-difference time-domain (FDTD) algorithm. However, complex geometries involving curved (such as conformal cathodes and curved waveguide sections) or very fine geometrical features cannot be accurately modeled by regular grids because of ensuing staircase (step-cell) effects. Although many studies have been done to ameliorate staircase errors in finite-differences, including the use of conformal finite-differences [18], [19], the most general solution to this problem is to employ irregular, unstructured grids (meshes). The finite-element (FE) method is a better option than FDTD in this case, because it is naturally suited for such type of grids. In addition, FE enables a greater degree of space-adaptivity (using mesh refinement techniques) in a systematic fashion and can also be applied for transient problems using FE time-domain (FETD) algorithms [20], [21].

However, existing FE-based EM-PIC codes based on unstructured grids have three important drawbacks. First, FE-based EM-PIC algorithms tend to numerically violate charge conservation due to the fact that the continuity equation leaves residuals at the discrete level on unstructured grids. Past efforts to enforce charge conservation have included adding a posterior correction steps by Poisson's solvers [16] or pseudocurrents [22]. However, the former approach requires a time-consuming linear solver at each time step and the latter introduces a diffusion parameter that may alter the physics. A recent charge-conserving PIC algorithm based on the second-order vector wave equation for the electric field that does not require introduction of correction terms is described in [23] and [24]. However, the solution space of the second-order vector wave equation in the time-domain includes spurious solutions with secular growth, of the form $t\nabla\phi$, which are not physical admissible solutions to Maxwell's equations and can pollute the numerical results [25]–[27]. More recently, a gather–scatter algorithm with exact charge conservation on unstructured grids was described in [25], based on concepts borrowed from differential geometry [28], [29] and discrete differential forms [30], [31]. Charge-conserving PIC algorithms were also developed under similar tenets in [32] and [33]. A second challenge for unstructured-grid EM-PIC algorithms is that the field solver is implicit, i.e., it requires the repeated solution of a linear system of equations sequentially at each time step [20]. Finally, a third challenge (shared by FDTD-based algorithms as well) is that their performance is hindered by the global Courant stability bounds on time steps used to advance fields and particles.

Manuscript received March 25, 2016; accepted June 11, 2016. Date of publication July 12, 2016; date of current version August 9, 2016. This work was supported in part by the National Science Foundation through the Division of Electrical, Communications and Cyber Systems under Grant 1305838 and in part by the Ohio Supercomputer Center under Grant PAS-0061 and Grant PAS-0110.

D.-Y. Na and F. L. Teixeira are with the Electro Science Laboratory, Department of Electrical and Computer Engineering, The Ohio State University, Columbus, OH 43212 USA (e-mail: na.94@osu.edu; teixeira.5@osu.edu).

H. Moon is with Intel corporation, Hillsboro, OR 97124 USA (e-mail: haksu00@gmail.com).

Y. A. Omelchenko is with Trinum Research Inc., San Diego, CA 92126 USA (e-mail: omelche@gmail.com).

Color versions of one or more of the figures in this paper are available online at http://ieeexplore.ieee.org.

Digital Object Identifier 10.1109/TPS.2016.2582143

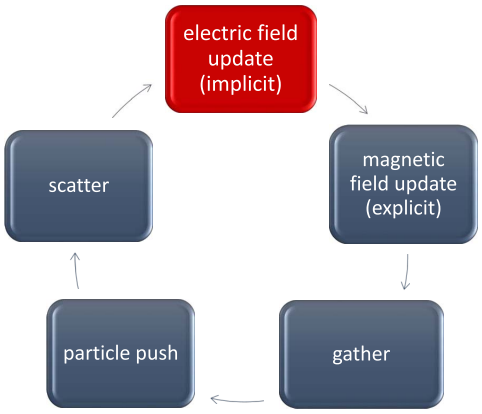

Fig. 1. Basic steps in a full-wave EM-PIC algorithm. On unstructured meshes, conventional field solvers for the electric field update are implicit, requiring the solution of a (large) linear system at each time step.

In order to overcome the second challenge noted earlier, a sparse approximate inverse (SPAI) strategy for unstructured meshes [34], [35] is incorporated here into an explicit FETD-based EM-PIC algorithm with exact charge-conserving properties developed in [25]. For a given mesh, the resulting SPAI explicit solver obtains an approximation for the inverse of the FE system matrix based on (powers of) the sparsity pattern of the original FE system matrix. This is done once-and-for all for any given mesh, i.e., independently of any field excitation and particle distribution, and decoupled from the field update. The SPAI explicit solver is easily parallelizable and produces exponential convergence of the approximate inverse matrix to the exact inverse matrix as the density (sparsity) of the former is increased (reduced) [34]. Importantly, since sparsity is retained, the algorithm remains local [35]. The explicit and the sparse nature of the resulting EM-PIC algorithm enables integration with asynchronous time-stepping techniques [36]–[38] designed to overcome the third challenge indicated earlier. We investigate in detail here the effect of the approximate inverse on the particle dynamics by comparing particle trajectories computed with the new proposed algorithm against analytical solutions (when available) and a conventional implicit EM-PIC algorithm employing a direct LU-solver. We show that the error caused by the SPAI approximation is several orders of magnitude smaller than inherent space and time discretization errors.

II. Explicit FETD-PIC Algorithm

A typical EM-PIC algorithm consists of four basic steps [25]: 1) field solver (consisting of electric and/or magnetic field updates from Maxwell's equations); 2) gather step (fields interpolation at each particle position); 3) scatter (assigning currents to grid edges and charges to grid nodes from the particle positions and velocities); and 4) particle acceleration and push (governed by Lorentz force and Newton's law of motion). These four steps are sequentially performed at each time step, as shown in Fig. 1.

A. Field Solver

In the language of differential forms for the electromagnetic field [39], the electric field E and the (Hodge dual of the) current density $\star J$ are represented as 1-forms, and the magnetic flux density B is represented as a 2-form. On a mesh, 1-forms and 2-forms are associated with mesh edges and faces, respectively [28], [29]. Accordingly, in order to discretize Maxwell's equations, the FETD algorithm expands E and $\star J$ in terms of Whitney 1-forms associated with the edges of the mesh, and B in terms of Whitney 2 forms associated with the faces of the mesh [25].

Next, using the generalized Stoke's theorem to obtain semi-discrete equations followed by a leap-frog discretization in time (second-order symplectic time integration), the following full-discrete FETD scheme is obtained [25], [34]:

$$\mathbb{B}^{n+\frac{1}{2}} = \mathbb{B}^{n-\frac{1}{2}} - \Delta t[\mathcal{D}_{\text{curl}}] \cdot \mathbb{E}^n \tag{1}$$

$$[\star_\epsilon] \cdot \mathbb{E}^{n+1} = [\star_\epsilon] \cdot \mathbb{E}^n + \Delta t\left([\mathcal{D}_{\text{curl}}]^T \cdot [\star_{\mu^{-1}}] \cdot \mathbb{B}^{n+\frac{1}{2}} - \mathbb{J}^{n+\frac{1}{2}}\right) \tag{2}$$

where Δt is the time step increment, the superscript n denotes the time step index, and $\mathbb{B}$, $\mathbb{E}$, and $\mathbb{J}$ are column vectors representing B on each face, and E and $\star J$ on each edge, respectively. In addition, $[\mathcal{D}_{\text{curl}}]$ is the incidence matrix representing the discrete exterior derivative (or, equivalently, the discrete curl operator distilled from the metric, that is, with elements in the set $\{-1, 0, 1\}$) on the mesh [28], [34], and $[\star_\epsilon]$ and $[\star_{\mu^{-1}}]$ are discrete Hodge (mass) matrices whose elements are given by the volume integrals [31], [34]

$$[\star_\epsilon]_{i,j} = \epsilon \int_\Omega \vec{W}_i^{(1)} \cdot \vec{W}_j^{(1)} d\Omega \tag{3}$$

$$[\star_{\mu^{-1}}]_{i,j} = \mu^{-1} \int_\Omega \vec{W}_i^{(2)} \cdot \vec{W}_j^{(2)} d\Omega \tag{4}$$

where $\vec{W}_i^{(1)}$, $i = 1 \ldots N_E$ and $\vec{W}_i^{(2)}$, $i = 1 \ldots N_F$ are the vector proxies of Whitney 1- and 2-forms [28] that span the set of N_E edges and N_F faces of the mesh, respectively. It can be shown that $[\mathcal{D}_{\text{curl}}]^T = [\mathcal{D}^*_{\text{curl}}]$, the incidence matrix on the dual mesh [25], [28], [29], [40], [41]. Equations (1) and (2) constitute an implicit field solver, because $[\star_\epsilon]$ is nondiagonal. In order to update the electric field from (2), it is necessary to solve a large linear system of equations at every time step. The explicit scheme proposed here is detailed in Section II-D.

B. Gather-Scatter and Particle Pusher Steps

In the gather step, Whitney forms are used to determine the electric and magnetic field values at the position of each particle, as shown schematically in Fig. 2(a). Specifically, from the values of $\mathbb{E}^n$ on edges and $\mathbb{B}^{n+(1/2)}$ and $\mathbb{B}^{n-(1/2)}$ on faces, vector proxies of Whitney forms are used to interpolate $\vec{E}^n(\vec{r})$ and $\vec{B}^n(\vec{r})$ at any ambient point $\vec{r}$, and in particular, at the charged particles' locations, by

$$\vec{E}^n(\vec{r}) = \sum_{i=1}^{N_E} [\mathbb{E}]_i^n \vec{W}_i^{(1)}(\vec{r}) \tag{5}$$

$$\vec{B}^n(\vec{r}) = \sum_{i=1}^{N_F} \frac{1}{2}\left([\mathbb{B}]_i^{n+\frac{1}{2}} + [\mathbb{B}]_i^{n-\frac{1}{2}}\right) \vec{W}_i^{(2)}(\vec{r}) \tag{6}$$

where $[\mathbb{E}]_i^n$ denotes the ith element of the column vector $\mathbb{E}^n$ and likewise for $[\mathbb{B}]_i^{n+(1/2)}$ and $[\mathbb{B}]_i^{n-(1/2)}$. This is shown schematically in Fig. 2(a). In the scatter step, we compute

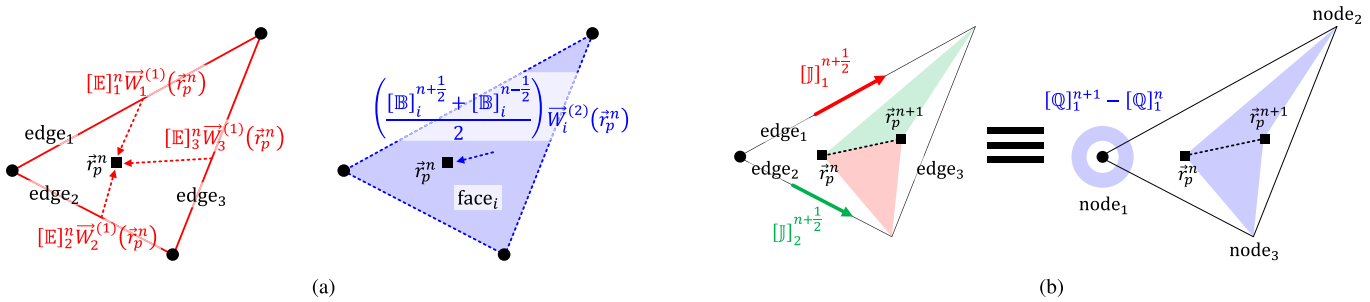

Fig. 2. Charge-conserving gather and scatter steps [25]. (a) Interpolation of $\vec{E}$ and $\vec{B}$ at the position of the particle by edge-based (left) and face-based degrees of freedom contributions (right) (weighted by the Whitney functions) in the gather step. (b) Exact charge-conserving scatter scheme. The sum of the two colored areas in the left, representing the magnitude of the edge currents, is equal to the blue area in the right, representing the charge variation at node 1 during one time step.

the particle current densities mapped to the edges of the mesh, i.e., to the mesh-based quantity $\mathbb{J}^{n+(1/2)}$, for incorporation back into the field solver. We adopt here the charge-conserving scatter for unstructured grids recently proposed in [25]. By referring to Fig. 2(b), given the initial $\vec{r}_p^{\,n}$ and final $\vec{r}_p^{\,n+1}$ locations of a particle p with charge q_p during a time step Δt, the associated current flowing along edge 1 is written as

$$[\mathbb{J}^n]_1 = \frac{q_p}{\Delta t}\int_{\vec{r}_p^{\,n}}^{\vec{r}_p^{\,n+1}} \vec{W}_1^{(1)}(\vec{r})\cdot d\vec{l} = \frac{q_p}{\Delta t}\left[\lambda_1(\vec{r}_p^{\,n})\lambda_2(\vec{r}_p^{\,n+1}) - \lambda_1(\vec{r}_p^{\,n+1})\lambda_2(\vec{r}_p^{\,n})\right] \quad (7)$$

where $\lambda_1(\vec{r})$ and $\lambda_2(\vec{r})$ are the barycentric coordinates of point $\vec{r}$ with respect to vertices 1 and 2, respectively, (the boundary points of edge 1 in consideration). Analogous assignments follow for the other edges of the mesh.

C. Discrete Continuity Equation

As demonstrated in [25], the above scatter algorithm yields exact charge conservation at the discrete level because the variation of the charge at any node of the mesh exactly matches the total current flowing in or out of that particular node. In other words, the following discrete continuity equation (DCE) holds:

$$\left[\mathcal{D}^*_{\text{div}}\right]\cdot\mathbb{J}^{n+\frac{1}{2}} + \frac{\mathbb{Q}^{n+1}-\mathbb{Q}^n}{\Delta t} = 0 \quad (8)$$

where $[\mathcal{D}^*_{\text{div}}]$ is the incidence matrix associated with the discrete divergence operator in the dual mesh, which is also equal to $[D_{\text{grad}}]^T$ [25], [28], [29], [40], [41], and $\mathbb{Q}^n$ denotes the column vector with the charge associated with each node of the mesh.[1] Note that the nodal charge at any node i is obtained from the sum of the nearby particle charges weighted by their corresponding barycentric coordinates with respect to that particular node, that is

$$[\mathbb{Q}]_i^n = \sum_p q_p \lambda_i(\vec{r}_p^{\,n}). \quad (9)$$

Barycentric coordinates can be identified as Whitney 0-forms associated with a particular node i, i.e., $W_i^{(0)}(\vec{r}_p^{\,n}) = \lambda_i(\vec{r}_p^{\,n})$ [28], [29]. We provide a geometrical illustration of (8) in Fig. 2(b). From (9), the charge variation at node 1 due to a charged particle movement during Δt is proportional to $\lambda_1(\vec{r}_p^{\,n+1}) - \lambda_1(\vec{r}_p^{\,n})$. This quantity is represented by the blue-colored area in Fig. 2(b). At the same time, from (7), the current flowing along edge 1 is associated with the factor $\lambda_1(\vec{r}_p^{\,n})\lambda_2(\vec{r}_p^{\,n+1}) - \lambda_1(\vec{r}_p^{\,n+1})\lambda_2(\vec{r}_p^{\,n})$, which is equal to the red-colored area in Fig. 2(b). A similar factor is present for edge 2, which is indicated by the green-colored area. From the area equivalences, it is clear that the sum of the current flow out of node 1 along edges 1 and 2 is equal to the charge variation on node 1.

The particle push step computes the Lorentz force acting on each charged particle given the (interpolated) electric and magnetic fields at the particle location and its velocity, and applies Newton's force law to accelerate the particle. This step is implemented here by extending the particle push described in [25] to the relativistic regime based on the methodology put forth in [42].

D. SPAI

As noted earlier, a linear solve (implicit time-update) is required in (2) due to the presence of $[\star_\epsilon]$ multiplying the unknown $\mathbb{E}^{n+1}$ on the left-hand side. Naively, this linear solve could be avoided by premultiplying both sides of (2) by $[\star_\epsilon]^{-1}$, leading to

$$\mathbb{E}^{n+1} = \mathbb{E}^n + \Delta t[\star_\epsilon]^{-1}\cdot\left(\left[\mathcal{D}^*_{\text{curl}}\right]\cdot[\star_{\mu^{-1}}]\cdot\mathbb{B}^{n+\frac{1}{2}} - \mathbb{J}^{n+\frac{1}{2}}\right). \quad (10)$$

This multiplication is, of course, wholly impractical for large problems, because $[\star_\epsilon]^{-1}$ is dense and such a direct inversion is computationally very costly and scales poorly with size. Even for relatively small problems, the fact that $[\star_\epsilon]^{-1}$ is dense makes the algorithm nonlocal and unsuited for asynchronous time-update algorithms [36]. Instead, to obtain an explicit and local field update algorithm, we explore the fact that, in the continuum, not only $\star_\epsilon$ but also $\star_\epsilon^{-1}$ are strictly local operators [31], [35], [43]. This indicates that, although dense, $[\star_\epsilon]^{-1}$ should be well approximated by a sparse approximate inverse (SPAI), which we denote $[\star_\epsilon]_a^{-1}$. Each column of $[\star_\epsilon]_a^{-1}$ can be obtained independently (and in parallel fashion) once a suitable sparsity pattern for $[\star_\epsilon]_a^{-1}$ is chosen. Since the sparsity pattern of $[\star_\epsilon]$ encodes the nearest-neighbor edge adjacency, good candidates for the sparsity pattern of $[\star_\epsilon]_a^{-1}$

[1]The equivalence between $[\mathcal{D}^*_{\text{div}}]$ and $[\mathcal{D}_{\text{grad}}]^T$, and similarly between $[\mathcal{D}^*_{\text{curl}}]$ and $[\mathcal{D}_{\text{curl}}]^T$ is up to a sign, depending on the relative orientation chosen for the primal and dual meshes [28].

are $[\star_\epsilon]^k$ for $k = 1, 2, \ldots$, which would encode k-nearest neighbor adjacency among edges (with larger k providing better accuracy but denser matrices). A parallel algorithm for computing $[\star_\epsilon]_a^{-1}$ along these lines is detailed in [34], where it is also shown that the Frobenius norm of the difference matrix $\|[\star_\epsilon]_a^{-1} - [\star_\epsilon]^{-1}\|_F$ has exponential convergence to zero for increasing k.

Once $[\star_\epsilon]_a^{-1}$ is precomputed, the explicit and local SPAI-based field update simply writes

$$\mathbb{E}^{n+1} = \mathbb{E}^n + \Delta t [\star_\epsilon]_{\mathrm{a}}^{-1} \cdot \left(\left[\mathcal{D}^*_{\mathrm{curl}}\right] \cdot [\star_{\mu^{-1}}] \cdot \mathbb{B}^{n+\frac{1}{2}} - \mathbb{J}^{n+\frac{1}{2}} \right). \tag{11}$$

E. Discrete Gauss' Law

By premultiplying both sides of (11) by $[\mathcal{D}^*_{\mathrm{div}}][\star_\epsilon]_a$, where $[\mathcal{D}^*_{\mathrm{div}}]$ is the incidence matrix representing the discrete divergence operator on the dual grid, and using the identity $[\mathcal{D}^*_{\mathrm{div}}] \cdot [\mathcal{D}^*_{\mathrm{curl}}] = 0$ [28], [29], [40], we obtain

$$\left[\mathcal{D}^*_{\mathrm{div}}\right] \cdot [\star_\epsilon]_a \cdot \mathbb{E}^{n+1} = \left[\mathcal{D}^*_{\mathrm{div}}\right] \cdot [\star_\epsilon]_a \cdot \mathbb{E}^n - \Delta t \left[\mathcal{D}^*_{\mathrm{div}}\right] \cdot \mathbb{J}^{n+\frac{1}{2}}. \tag{12}$$

This last equation can be rearranged as

$$\left[\mathcal{D}^*_{\mathrm{div}}\right] \cdot [\star_\epsilon]_a \cdot \left(\frac{\mathbb{E}^{n+1} - \mathbb{E}^n}{\Delta t} \right) = -\left[\mathcal{D}^*_{\mathrm{div}}\right] \cdot \mathbb{J}^{n+\frac{1}{2}} \tag{13}$$

which, using (8), can be rewritten as

$$\left[\mathcal{D}^*_{\mathrm{div}}\right] \cdot [\star_\epsilon]_a \cdot \left(\frac{\mathbb{E}^{n+1} - \mathbb{E}^n}{\Delta t} \right) = \frac{\mathbb{Q}^{n+1} - \mathbb{Q}^n}{\Delta t}. \tag{14}$$

Equation (14) implies that the residuals of the discrete Gauss' law (DGL) at any two successive time steps remain the same, in other words

$$\left[\mathcal{D}^*_{\mathrm{div}}\right] \cdot [\star_\epsilon]_a \cdot \mathbb{E}^{n+1} - \mathbb{Q}^{n+1} = \left[\mathcal{D}^*_{\mathrm{div}}\right] \cdot [\star_\epsilon]_a \cdot \mathbb{E}^n - \mathbb{Q}^n \tag{15}$$

and by induction

$$\underbrace{\left[\mathcal{D}^*_{\mathrm{div}}\right] \cdot [\star_\epsilon]_a \cdot \mathbb{E}^n - \mathbb{Q}^n}_{\mathrm{res}^n} = \underbrace{\left[\mathcal{D}^*_{\mathrm{div}}\right] \cdot [\star_\epsilon]_a \cdot \mathbb{E}^0 - \mathbb{Q}^0}_{\mathrm{res}^0} \tag{16}$$

for all n, so that if initial conditions have $[\mathcal{D}^*_{\mathrm{div}}] \cdot [\star_\epsilon]_a \cdot \mathbb{E}^0 = \mathbb{Q}^0$, then the DGL is verified for all time steps.

In Section III, we analyze the error incurred by the above-mentioned SPAI approximation to obtain an explicit field solver for EM-PIC simulations on unstructured grids.

III. Numerical Results and Discussion

In order to investigate the error caused by the SPAI-based explicit solver in EM-PIC simulations, we consider in this section examples involving single charged-particle trajectories, a plasma ball expansion, and an accelerated electron beam.

A. Single-Particle Trajectories

Typical PIC simulations comprise an ensemble of superparticles effecting a coarse-graining of the phase-space. As such, instantaneous errors in individual particle trajectories may not always be relevant when computing grid-averaged physical quantities. Nevertheless, it is of interest to examine the secular trends on the particle trajectory discrepancies.

We investigate the motion of a single charged particle initially positioned at the origin in the presence of an external magnetic field B_z^{ext} and electric field E_y^{ext}. In this case, the exact solution can be written as [44]

$$\begin{aligned} x(t) &= \frac{v_{y,0}}{\omega_c} \cos \omega_c t + \left(\frac{v_{x,0}}{\omega_c} + \frac{q_p E_y^{\mathrm{ext}}}{m_p \omega_c^2} \right) \sin \omega_c t \\ &\quad - \left(\frac{q_p E_y^{\mathrm{ext}}}{m_p \omega_c^2} t + \frac{v_{y,0}}{\omega_c} \right) \\ y(t) &= \frac{v_{y,0}}{\omega_c} \sin \omega_c t - \left(\frac{v_{x,0}}{\omega_c} + \frac{q_p E_y^{\mathrm{ext}}}{m_p \omega_c^2} \right) \cos \omega_c t \\ &\quad + \left(\frac{q_p E_y^{\mathrm{ext}}}{m_p \omega_c^2} + \frac{v_{y,0}}{\omega_c} \right) \end{aligned} \tag{17}$$

where $v_{x,0}$ and $v_{y,0}$ are the initial velocity components.

We examine two types of single-particle trajectories. The first corresponds a pure cyclotron motion ($B_z \neq 0$ and $E_y = 0$) and the second includes a drift motion as well ($B_z \neq 0$ and $E_y \neq 0$). We assume a superparticle with $q_p = -1.6 \times 10^{-15}$ [C] and mass $m_p = 9.1 \times 10^{-27}$ [kg]. In both cases, the initial velocity is set equal to 2×10^8 [m/s].

TABLE I
Number of Elements in Meshes 1, 2, and 3

	Mesh 1	Mesh 2	Mesh 3
Edge #	951	2168	6036
Face #	610	1408	3960
Node #	342	761	2077
Δl_{av} [m]	0.1160	0.0590	0.0300

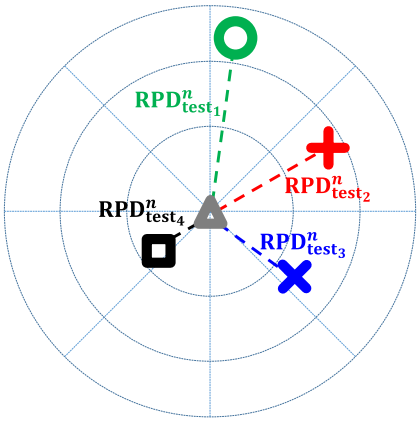

(a)

Fig. 3. RPD of the various test particles with respect to the standard particle placed at the origin, in a polar diagram where the radial distance is represented in logarithmic scale.

TABLE II
Convention Used for Particle Trajectory Visualization

solver	test particle number	symbol used
analytical sol.	1	○
SPAI $k = 2$	2	+
SPAI $k = 4$	3	×
SPAI $k = 6$	4	□

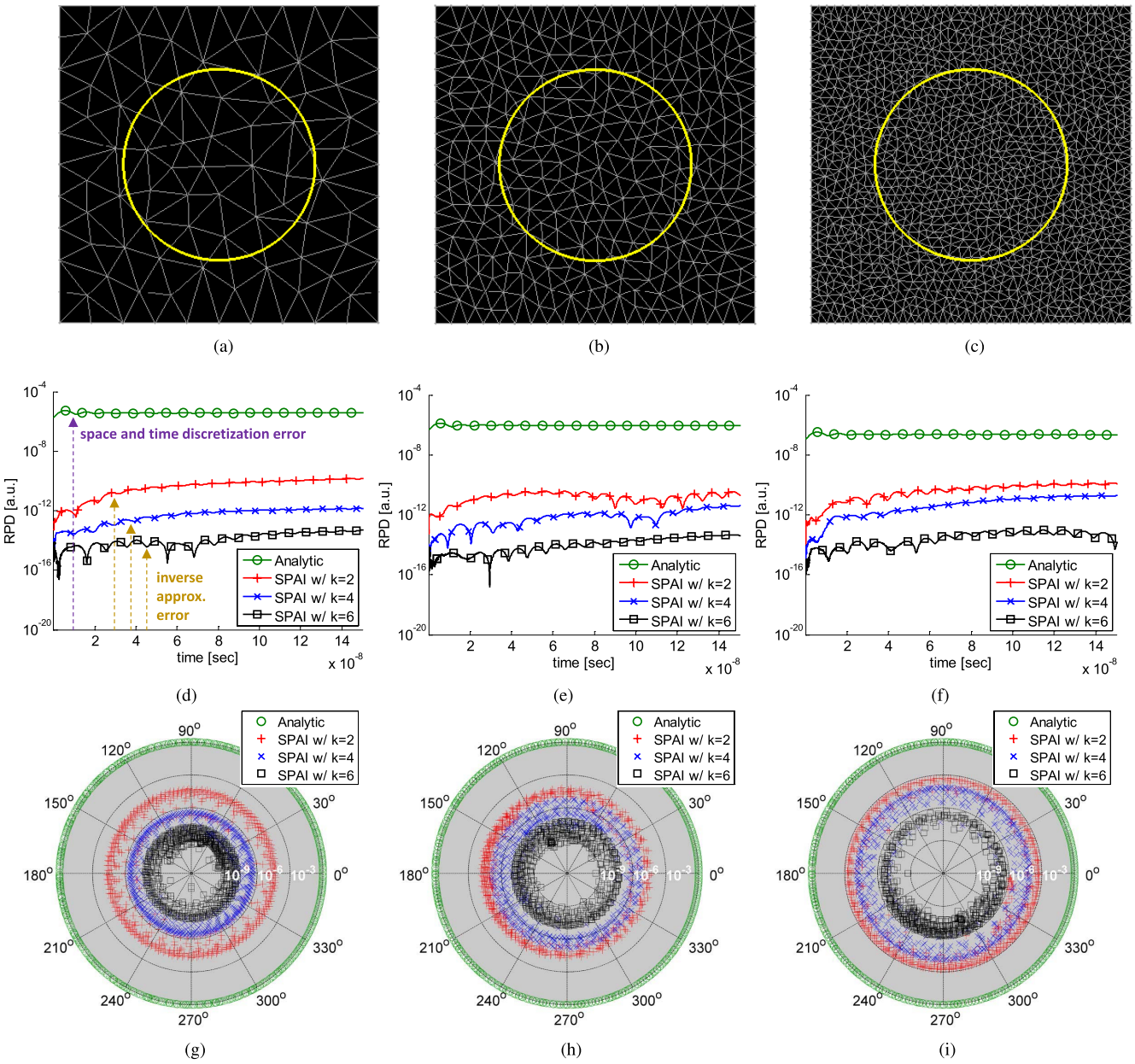

Fig. 4. Results for a circular particle trajectory on three different meshes. (a)–(c) Particle trajectory histories. (d)–(f) RPDs versus time for the four test particles. (g)–(i) Normalized RPD bands for the four test particles.

We consider three unstructured meshes labeled, from coarsest to finest, as 1, 2, and 3, all of which discretize the domain $\Omega = \{(x, y) \in [0, 1]^2\}$. Table I provides information about the number of elements and other properties of the meshes considered. The parameter Δl_{av} indicates the average edge length, which roughly halves for each mesh index increment.

The boundaries of the solution domain are truncated using a perfectly matched layer (PML) [26], [27], [45]. The time increment is chosen as $\Delta t = 10$, 5, and 2.5 [ps] for meshes 1, 2, and 3, respectively, and the simulation is terminated at $t = 150$ [ns].

An implicit solver based on an LU decomposition is used as reference. Charged-particle trajectories calculated by using such LU-solver are referred to as standard trajectories. On the other hand, particle trajectories obtained by the SPAI-based explicit field solver are designated as test trajectories. The effect of the inverse approximation error can be quantified by examining the discrepancy between the standard and test trajectories. This discrepancy can be further compared with the discrepancy in particles' trajectories between the result from the LU-based solver and the analytic solution, which measures the inherent numerical (space and time) discretization error.

To quantify the error, we define the relative position difference (RPD) that is the ratio of the magnitude of the difference between the standard and test position vectors at certain time step n to the total travel length of the standard particle up to

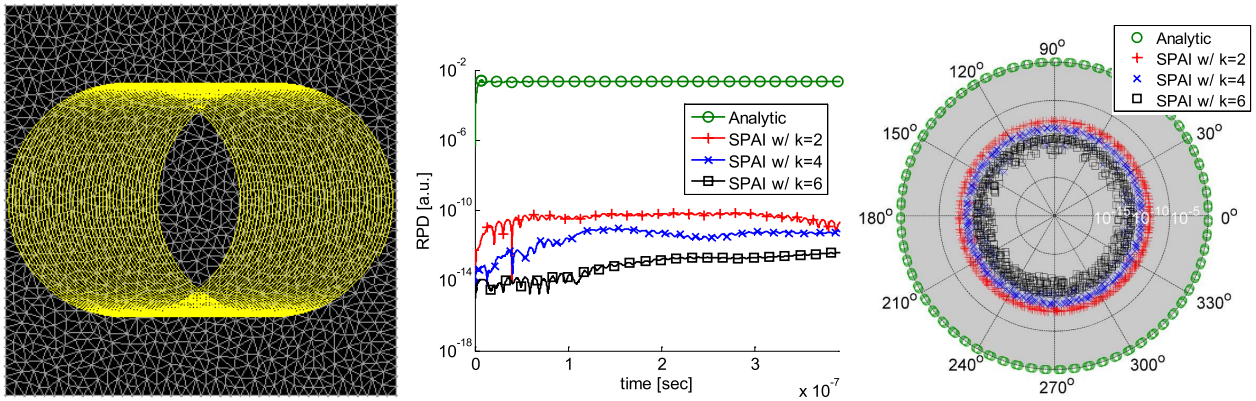

(a) (b) (c)

Fig. 5. Results for a trajectory with drift. (a) Particle trajectory history. (b) RPDs versus time for the four test particles. (c) Normalized RPD bands for the four test particles.

time step n, that is

$$\mathrm{RPD}^n_{\mathrm{test}_j} = \frac{\left|\vec{r}^{\,n}_{p,\mathrm{test}_j} - \vec{r}^{\,n}_{p,\mathrm{std}}\right|}{\sum_{i=1}^{n}\left|\vec{r}^{\,i}_{p,\mathrm{std}} - \vec{r}^{\,i-1}_{p,\mathrm{std}}\right|} = \frac{|\vec{d}^{\,n}_{\mathrm{test}_j}|}{L_{\mathrm{std}}} \tag{18}$$

where $\mathrm{RPD}^n_{\mathrm{test}_j}$ is the RPD for the jth test particle at time instant n, and $\vec{r}^{\,i}_{p,\mathrm{std}}$ and $\vec{r}^{\,i}_{p,\mathrm{test}_j}$ are the standard and test particle position, respectively, at time step i.

For visualization purposes, we plot the RPD in a polar graph as shown in Fig. 3, with the radial coordinate represented in a logarithmic scale. The standard trajectory points computed by the implicit LU-based solver are indicated by △ and placed at the origin of the RPD for all times. The symbols ◯, +, ×, and □ represent, in turn, the relative position of test particles' 1, 2, 3, and 4 with respect to the standard trajectory points, as given by the vector $\vec{d}^{\,n}_{\mathrm{test}_j}/L_{\mathrm{std}}$. As summarized in Table II, these four sets of points correspond, respectively, to the exact trajectory points obtained via an analytic solution and to the trajectory points obtained using the SPAI-based explicit field solver with $k = 2$, 4, and 6.

1) Circular Trajectory: In this case, $B_z^{\mathrm{ext}} = 5.085 \times 10^{-3}$ [Wb/m^2] and $E_y^{\mathrm{ext}} = 0$ [V/m] so that a pure cyclotron motion with angular frequency $\omega_c = 6.05 \times 10^2$ [rad/s] results. Fig. 4 shows the result of the SCP test for the circular trajectory. Fig. 4(a)–(c) shows the trajectory of the SCP for meshes 1, 2, and 3, respectively. Fig. 4(d)–(f) shows the RPDs for four test particles on each mesh. It is seen that the RPDs for the analytic test particle are very large (several orders of magnitude) compared with the RPDs of the EM-PIC simulation with SPAI-based explicit field solver for $k = 2$, 4, and 6. We note again that the RPD for the analytic test particle arises from the space and time discretization errors, whereas the other RPDs are due solely to the inverse approximation error. Therefore, these results indicate that inverse approximation error is negligible compared with the other inherent numerical errors. We also note, as expected, that the RPD due to the discretization error decreases as the mesh is progressively refined [curve with ◯ in Fig. 4(d)–(f)]. On the other hand, the RPD due to the inverse approximation error remains fairly constant across the different meshes [curves with +, ×, and □ in Fig. 4(d)–(f)]. Examining these figures, it is also observed that the error decreases as the parameter k increases.

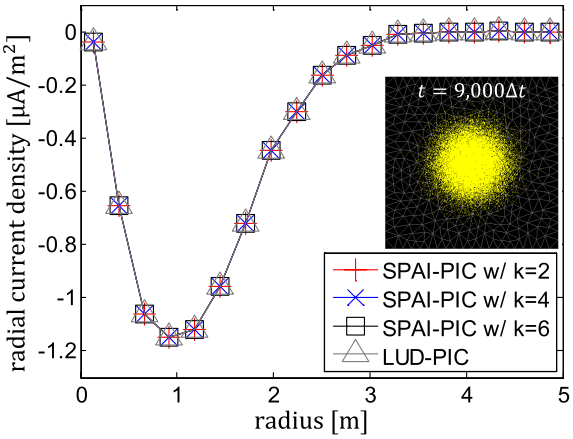

Fig. 6. Radial current versus radius coordinate for the expanding plasma at time step $n = 9 \times 10^4$ using the LU-based implicit fields solver and the SPAI-based explicit field solver with $k = 2$, 4, and 6.

Fig. 4(g)–(i) shows the RPD bands normalized by the analytic test particle's RPD (i.e., setting the RPD of the analytical result to unity radius in the plot). In all cases, the normalized RPD bands rotate around the origin (LU-decomposition implicit solution) around nearly circular orbits. Such normalized RPD bands for test particles 2, 3, and 4 become larger as mesh is refined, since the space and time discretization errors decrease, as noted earlier.

2) Trajectory With Drift: In this case, we set $B_z^{\mathrm{ext}} = 5.085 \times 10^{-3}$ [Wb/m^2] and $E_y^{\mathrm{ext}} = -5 \times 10^3$ [V/m]. This add a drift motion to the trajectory of the particle, as shown in Fig. 5(a). We consider mesh 3 result only, for brevity. The RPD data are shown in Fig. 5(b) and (c). Similar to the pure circular trajectory case, the RPDs for different values of k are very small compared with analytic RPD. It is again seen that the bands converge to the center of the circle, which stands for the position of the standard particle, as k increases.

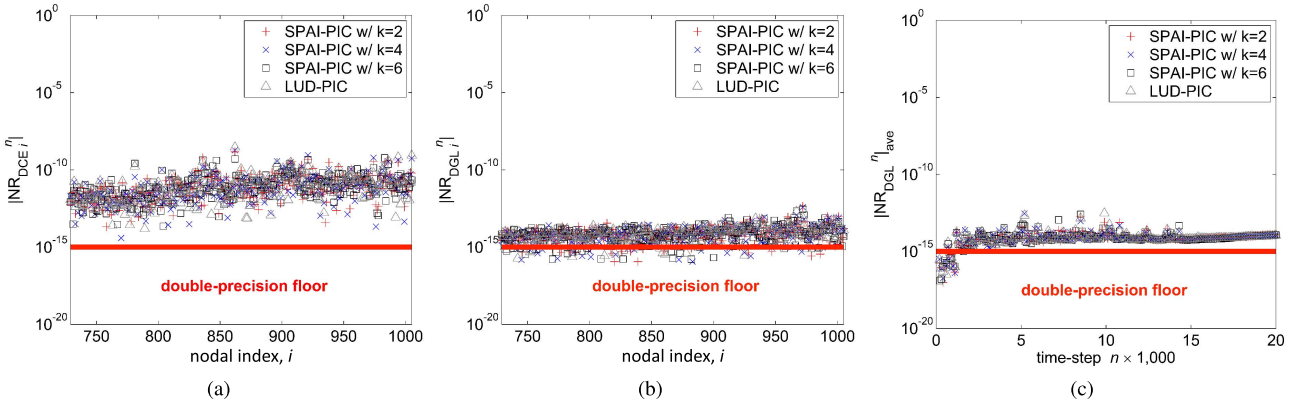

Fig. 7. (a) NRs of the DCE for the plasma ball expansion example using different field solvers, at $t = 2 \times 10^4 \Delta t$. (b) Similar results for the DGL. (c) Averaged NRs for the DGL versus time step index.

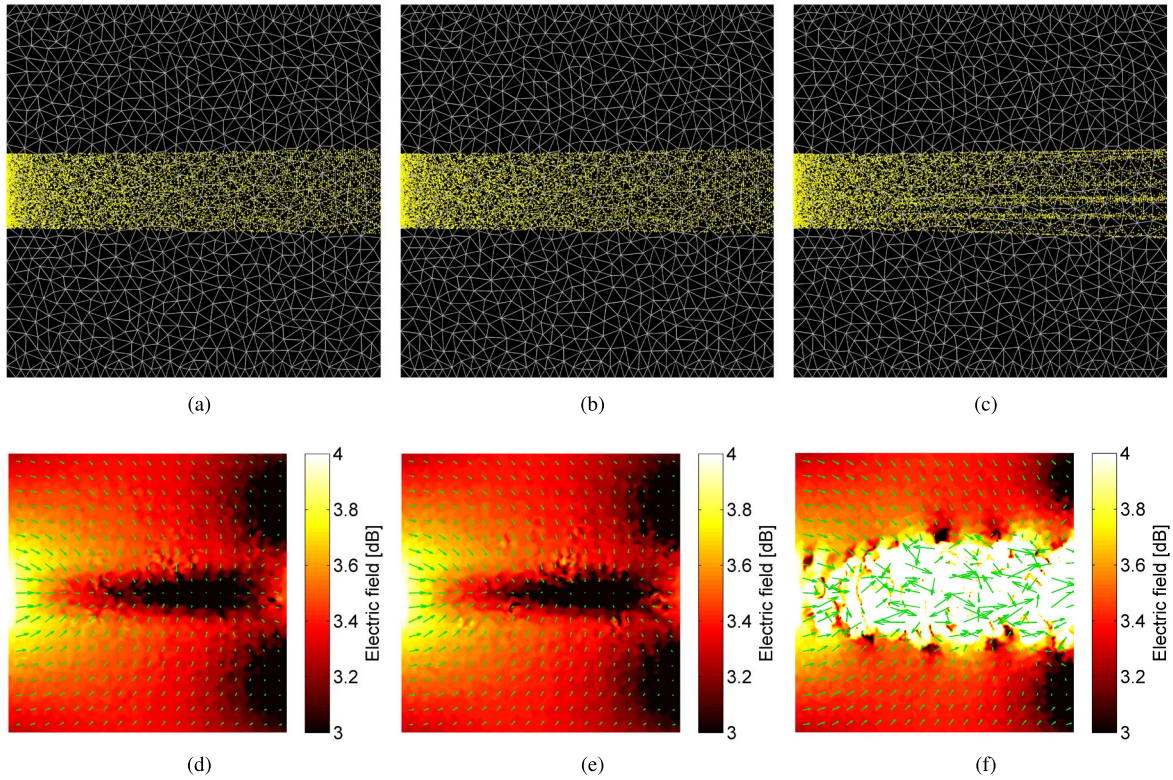

Fig. 8. Results for the accelerated electron beam at $t = 6 \times 10^4 \Delta t$. (a) and (b) Particle distribution snapshot from charge-conserving EM-PIC algorithms using an LU-based implicit solver and an SPAI-based ($k = 2$) explicit solver. (c) Particle distribution snapshot from a conventional (noncharge conserving on the unstructured grid) EM-PIC algorithm with an LU-based implicit solver. (d)–(f) Corresponding electric-field profile distributions.

B. Plasma Ball Expansion

In the next example, we consider the simulation of an expanding plasma ball. We consider 5×10^4 superparticles, each representing 200 electrons, initially placed uniformly within a circle of 0.5 [m] radius centered at the origin. At $t = 0$, the positive and negative charged particles overlap with net zero charge everywhere. Negative particles are initialized with Maxwellian distribution with thermal velocity $|\vec{v}_{\text{th}}| = 0.1 \times c$ [m/s]. Positive charged are assumed with zero velocity at all times. The initial density of particles is $n \approx 6.37 \times 10^4$ [m^{-3}] and the Debye length is $\lambda_D \approx 0.663$ [m], resulting on a plasma parameter $\Lambda = 4\pi n \lambda_d \approx 2.34 \times 10^5$. The unstructured mesh used in this simulation has 1880 faces, 2884 edges, and 1005 nodes. A PML is used to truncate the solution domain. A time step increment $\Delta t = 5$ [ps] is used, and the simulation is terminated at 10 [ns].

Fig. 6 shows the radial current density from the plasma expansion at $t = 9 \times 10^3 \Delta t$ as a function of the radial coordinate computed by implicit LU-based and explicit SPAI-based field solvers with $k = 2$, 4, and 6. Fig. 6 (inset) shows a snapshot of the particle distribution at $t = 9 \times 10^3 \Delta t$. There is no discernible difference in the current density profile among the results shown in Fig. 6.

In order to check charge conservation, we plot in Fig. 7(a) the NR for DCE (8) and DGL (14). These residuals are evaluated for each time step $n + (1/2)$ or n and node i,

and defined as

$$\mathrm{NR}_{\mathrm{DCE}_i}^{n+\frac{1}{2}} = 1 + \frac{\frac{[\mathbb{Q}]_i^{n+1} - [\mathbb{Q}]_i^n}{\Delta t}}{\sum_{j=1}^{N_e} \left[\mathcal{D}_{\mathrm{div}}^*\right]_{i,j} [\mathbb{J}]_j^{n+\frac{1}{2}}} \tag{19}$$

$$\mathrm{NR}_{\mathrm{DGL}_i}^{n} = 1 - \frac{[\mathbb{Q}]_i^n}{\sum_{j=1}^{N_v} \left[\mathcal{D}_{\mathrm{div}}^*\right]_{i,j} \left(\sum_{k=1}^{N_e} [\star_\epsilon]_{a\,j,k} [\mathbb{E}]_k^n\right)} \tag{20}$$

where N_v denotes the total number of nodes in the mesh. Fig. 7(a) shows $|\mathrm{NR}_{\mathrm{DCE}_i}^{n+(1/2)}|$ at $n = 20\,000$ versus the nodal index for different solvers. As seen, $|\mathrm{NR}_{\mathrm{DCE}_i}^{n+(1/2)}|$ is fairly low, about 10^{-13}, in all cases. The small noise above the double-precision floor 10^{-15} can be attributed from arithmetic round-off errors in the scatter process. Fig. 7(b) shows a similar plot now for $|\mathrm{NR}_{\mathrm{DGL}_i}^{n}|$, which is very close to the double-precision floor. In order to verify that residual levels of the DGL are maintained by (16) during the time-update, we also plot $|\mathrm{NR}_{\mathrm{DGL}_i}^{n}|$ averaged across all the nodes of the mesh, i.e., $|\mathrm{NR}_{\mathrm{DGL}}^{n}|_{\mathrm{ave}} = \sum_{i=1}^{N_v} \mathrm{NR}_{\mathrm{DGL}_i}^{n}/N_v$ as a function of the time step n in Fig. 7(c). As seen, $|\mathrm{NR}_{\mathrm{DGL}}^{n}|_{\mathrm{ave}}$ has nearly constant values close to the double-precision floor, with only a very small increase due to cumulative round-off error.

C. Electron Beam

In order to further verify charge conservation and stability for long-time simulations, we simulate next an electron beam accelerated by a vacuum diode. The domain $\Omega = \{(x, y) \in [0, 1]^2\}$ has lateral walls representing anode and cathode surfaces with potential difference set as 1.5×10^5 V. The top and bottom boundaries of the domain are truncated by a PML. The unstructured mesh has 2301 faces, 3524 edges, and 1224 nodes. The time step interval is set to $\Delta t = 270$ [ps], and the simulation is run up to 16.2 [μs]. Each superparticle used in the simulation represents 50×10^6 electrons. For the thermionic emission of electrons from the cathode at the left boundary, a slow initial mean velocity of 10^4 [m/s] is assumed for the electrons. Fig. 8 shows snapshots of the particle distribution and the self-field (electric) profile. Fig. 8(a) and (d) shows the field and particle distribution for the charge-conserving EM-PIC algorithm with LU-based implicit field solver. Fig. 8(b) and (e) shows the field and particle distribution for the charge-conserving EM-PIC algorithm with SPAI-based ($k = 2$) explicit field solver. Finally, Fig. 8(c) and (f) shows the field and particle distribution for an EM-PIC with LU-based implicit field solver and conventional gather step (noncharge-conserving on an unstructured grid) where edge currents are obtained from the straightforward projection of the instantaneous product $q\vec{v}$, summed over all particles, onto the edge element $\vec{W}_i^{(1)}$, that is

$$[\mathbb{J}]_i^{n+\frac{1}{2}} = \sum_p q_p \vec{v}_p^{\,n+\frac{1}{2}} \cdot \vec{W}_i^{(1)}\left(\vec{r}_p^{\,n+\frac{1}{2}}\right) \tag{21}$$

where $\vec{r}_p^{\,n+(1/2)} = (\vec{r}_p^{\,n+1} + \vec{r}_p^{\,n})/2$. In the latter case, violation of the continuity equation produced spurious bunching of the charges into strips of higher density. In addition, the self-field is highly asymmetric and randomly oriented near the beam center. These spurious effects are not present in either the implicit or the explicit charge-conserving simulations.

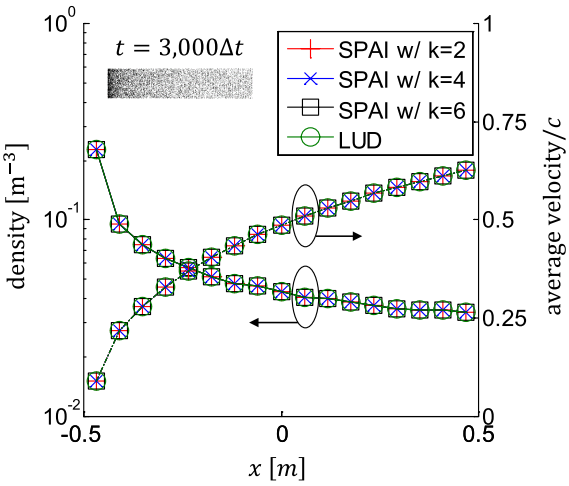

Fig. 9. Number density and average velocity of particles across a transversal section of the electron beam at $t = 3 \times 10^3\,\Delta t$, after steady state has been reached.

Fig. 9 shows the average particle density and the average velocity of particles across a transverse section of the beam versus the longitudinal direction x along the beam at time step $n = 3000$, for the charge-conserving algorithm with LU-based implicit solver and with SPAI-based explicit solver using $k = 2, 4, 6$. As expected, the number density of particles monotonically decreases as the average velocity of particles increases, keeping a uniform current flow in steady state across x. There is excellent agreement among all these cases, indicating the robustness of the SPAI-based explicit solver.

IV. Conclusion

We have developed an EM-PIC algorithm suited for unstructured grids, which combines a local explicit field solver with a charge-conserving scatter–gather scheme. A sparse approximate inverse is precomputed to obviate the need for a linear solver at each time step and to retain the local nature of the algorithm. Excellent agreement was verified between EM-PIC simulations utilizing the proposed field solver and a conventional (implicit) field solver based on an LU-solver. The explicit and local nature of the proposed EM-PIC algorithm makes it suitable for integration with asynchronous time-stepping techniques as well.

References

[1] C. K. Birdsall and A. B. Langdon, *Plasma Physics Via Computer*, 1st ed. New York, NY, USA: McGraw-Hill, 1985.
[2] R. W. Hockney and J. W. Eastwood, *Computer Simulation Using Particles*, 1st ed. Bristol, U.K.: CRC Press, 1988.
[3] Y. N. Grigoryev, V. A. Vshivkov, and M. P. Fedoruk, *Numerical 'Particle-in-Cell' Methods: Theory and Applications*. Berlin, Germany: De Gruyter, 2002.
[4] E. Esarey, P. Sprangle, J. Krall, and A. Ting, "Overview of plasma-based accelerator concepts," *IEEE Trans. Plasma Sci.*, vol. 24, no. 2, pp. 252–288, Apr. 1996.
[5] D. L. Bruhwiler *et al.*, "Particle-in-cell simulations of plasma accelerators and electron-neutral collisions," *Phys. Rev. ST Accel. Beams*, vol. 4, p. 101302, Oct. 2001.

[6] C. Huang *et al.*, "QUICKPIC: A highly efficient particle-in-cell code for modeling wakefield acceleration in plasmas," *J. Comput. Phys.*, vol. 217, no. 2, pp. 658–679, 2006.
[7] S. F. Martins, R. A. Fonseca, W. Lu, W. B. Mori, and L. O. Silva, "Exploring laser-wakefield-accelerator regimes for near-term lasers using particle-in-cell simulation in Lorentz-boosted frames," *Nature Phys.*, vol. 6, pp. 311–316, Mar. 2010.
[8] D. J. Strozzi *et al.*, "Fast-ignition transport studies: Realistic electron source, integrated particle-in-cell and hydrodynamic modeling, imposed magnetic fields," *Phys. Plasmas*, vol. 19, no. 7, p. 072711, 2012.
[9] C. Bellei *et al.*, "Fast ignition: Dependence of the ignition energy on source and target parameters for particle-in-cell-modelled energy and angular distributions of the fast electrons," *Phys. Plasmas*, vol. 20, no. 5, p. 052704, 2013.
[10] A. V. Elzhov *et al.*, "JINR activity in microwave sources for TeV range linear colliders," *Problems Atom. Sci. Technol.*, no. 2, pp. 103–106, 2000.
[11] R. Zheng, P. Ohlckers, and X. Chen, "Particle-in-cell simulation and optimization for a 220-GHz folded-waveguide traveling-wave tube," *IEEE Trans. Electron Devices*, vol. 58, no. 7, pp. 2164–2171, Jul. 2011.
[12] Z.-H. Li, "Investigation of an oversized backward wave oscillator as a high power microwave generator," *Appl. Phys. Lett.*, vol. 92, no. 5, p. 054102, 2008.
[13] F. Xie, G. Wen, J. Li, and S. Liu, "Particle-in-cell simulations from a X band coaxial relativistic backward wave oscillator," *Int. J. Infr. Millim. Waves*, vol. 19, no. 7, pp. 1037–1044, 1998.
[14] S. H. Gold and G. S. Nusinovich, "Review of high-power microwave source research," *Rev. Sci. Instrum.*, vol. 68, no. 11, pp. 3945–3974, 1997.
[15] E. Schamiloglu, "High power microwave sources and applications," in *IEEE MTT-S Int. Microw. Symp. Dig.*, vol. 2. Jun. 2004, pp. 1001–1004.
[16] J. W. Eastwood, "The virtual particle electromagnetic particle-mesh method," *Comput. Phys. Commun.*, vol. 64, no. 2, pp. 252–266, 1991.
[17] T. Umeda, Y. Omura, T. Tominaga, and H. Matsumoto, "A new charge conservation method in electromagnetic particle-in-cell simulations," *Comput. Phys. Commun.*, vol. 156, no. 1, pp. 73–85, 2003.
[18] C. S. Meierbachtol, A. D. Greenwood, J. P. Verboncoeur, and B. Shanker, "Conformal electromagnetic particle in cell: A review," *IEEE Trans. Plasma Sci.*, vol. 43, no. 11, pp. 3778–3793, Nov. 2015.
[19] J. Loverich, C. Nieter, D. Smithe, S. Mahalingam, and P. Stoltz, "Charge conserving emission from conformal boundaries in electromagnetic PIC simulations," 2009. [Online]. Available: http://www.john-loverich.com/emission.pdf
[20] F. L. Teixeira, "Time-domain finite-difference and finite-element methods for Maxwell equations in complex media," *IEEE Trans. Antennas Propag.*, vol. 56, no. 8, pp. 2150–2166, Aug. 2008.
[21] J.-F. Lee, R. Lee, and A. Cangellaris, "Time-domain finite-element methods," *IEEE Trans. Antennas Propag.*, vol. 45, no. 3, pp. 430–442, Mar. 1997.
[22] B. Marder, "A method for incorporating Gauss' law into electromagnetic PIC codes," *J. Comput. Phys.*, vol. 68, no. 1, pp. 48–55, 1987.
[23] A. Candel *et al.*, "Parallel finite element particle-in-cell code for simulations of space-charge dominated beam-cavity interactions," in *Proc. IEEE Particle Accel. Conf.*, Albuquerque, NM, USA, Jun. 2007, pp. 908–910.
[24] A. Candel *et al.*, "Parallel higher-order finite element method for accurate field computations in wakefield and PIC simulations," SLAC, Menlo Park, CA, USA, Tech. Rep. SLAC-PUB-13667, 2009.
[25] H. Moon, F. L. Teixeira, and Y. A. Omelchenko, "Exact charge-conserving scatter–gather algorithm for particle-in-cell simulations on unstructured grids: A geometric perspective," *Comput. Phys. Commun.*, vol. 194, pp. 43–53, Sep. 2015.
[26] B. Donderici and F. L. Teixeira, "Mixed finite-element time-domain method for transient Maxwell equations in doubly dispersive media," *IEEE Trans. Microw. Theory Techn.*, vol. 56, no. 1, pp. 113–120, Jan. 2008.
[27] B. Donderici and F. L. Teixeira, "Conformal perfectly matched layer for the mixed finite element time-domain method," *IEEE Trans. Antennas Propag.*, vol. 56, no. 4, pp. 1017–1026, Apr. 2008.
[28] F. L. Teixeira and W. C. Chew, "Lattice electromagnetic theory from a topological viewpoint," *J. Math. Phys.*, vol. 40, no. 1, pp. 169–187, 1999.
[29] F. L. Teixeira, "Lattice Maxwell's equations," *Prog. Electromagn. Res.*, vol. 148, pp. 113–128, Jul. 2014.
[30] B. He and F. L. Teixeira, "On the degrees of freedom of lattice electrodynamics," *Phys. Lett. A*, vol. 336, no. 1, pp. 1–7, 2005.
[31] B. He and F. L. Teixeira, "Geometric finite element discretization of Maxwell equations in primal and dual spaces," *Phys. Lett. A*, vol. 349, pp. 1–14, Jan. 2006.
[32] J. Squire, H. Qin, and W. M. Tang, "Geometric integration of the Vlasov–Maxwell system with a variational particle-in-cell scheme," *Phys. Plasmas*, vol. 19, no. 8, p. 084501, 2012.
[33] M. Campos-Pinto, S. Jund, S. Salmon, and E. Sonnendrücker, "Charge-conserving FEM–PIC schemes on general grids," *Comp. Rendus Mécanique*, vol. 342, pp. 570–582, Oct./Nov. 2014.
[34] J. Kim and F. L. Teixeira, "Parallel and explicit finite-element time-domain method for Maxwell's equations," *IEEE Trans. Antennas Propag.*, vol. 59, no. 6, pp. 2350–2356, Jun. 2011.
[35] B. He and F. L. Teixeira, "Differential forms, Galerkin duality, and sparse inverse approximations in finite element solutions of Maxwell equations," *IEEE Trans. Antennas Propag.*, vol. 55, no. 5, pp. 1359–1368, May 2007.
[36] Y. A. Omelchenko and H. Karimabadi, "Self-adaptive time integration of flux-conservative equations with sources," *J. Comput. Phys.*, vol. 216, pp. 179–194, Jul. 2006.
[37] H. Karimabadi, J. Driscoll, Y. A. Omelchenko, and N. Omidi, "A new asynchronous methodology for modeling of physical systems: Breaking the curse of Courant condition," *J. Comput. Phys.*, vol. 205, pp. 755–775, May 2005.
[38] Y. A. Omelchenko and H. Karimabadi, "Event-driven, hybrid particle-in-cell simulation: A new paradigm for multi-scale plasma modeling," *J. Comput. Phys.*, vol. 216, pp. 153–178, Jul. 2006.
[39] C. W. Misner, K. S. Thorne, and J. A. Wheeler, *Gravitation*. San Francisco, CA, USA: Freeman, 1973.
[40] M. Clemens and T. Weiland, "Discrete electromagnetism with the finite integration technique," in *Proc. Prog. Electromagn. Res.*, vol. 32. 2001, pp. 65–87.
[41] P. B. Bochev and J. M. Hyman, "Principles of mimetic discretizations of differential operators," in *Compatible Spatial Discretizations* (The IMA Volumes in Mathematics and Its Applications), vol. 142. New York, NY, USA: Springer, 2006, pp. 89–119.
[42] J.-L. Vay, "Simulation of beams or plasmas crossing at relativistic velocity," *Phys. Plasmas*, vol. 15, no. 5, p. 056701, 2008.
[43] A. Gillette and C. Bajaj, "Dual formulations of mixed finite element methods with applications," *Comput.-Aided Design*, vol. 43, pp. 1213–1221, Oct. 2011.
[44] M. Moisan and J. Pelletier, "Individual motion of a charged particle in electric and magnetic fields," in *Physics of Collisional Plasmas: Introduction to High-Frequency Discharges*. Dordrecht, The Netherlands: Springer, 2012, ch. 2, pp. 101–202.
[45] F. L. Teixeira and W. C. Chew, "General closed-form PML constitutive tensors to match arbitrary bianisotropic and dispersive linear media," *IEEE Microw. Guided Wave Lett.*, vol. 8, no. 6, pp. 223–225, Jun. 1998.

Dong-Yeop Na (S'09) received the B.S. and M.S. degrees in electrical engineering from Ajou University, Suwon, South Korea, in 2012 and 2014, respectively. He is currently pursuing the Ph.D. degree in electrical engineering with The Ohio State University, Columbus, OH, USA.

He is a Graduate Research Associate with the Electro-Science Laboratory, The Ohio State University. His current research interests include computational electromagnetics and charged particle dynamics.

Haksu Moon received the B.S. degree from Hanyang University, Seoul, South Korea, in 2008, and the M.S. and Ph.D. degrees from the Electro-Science Laboratory, The Ohio State University, Columbus, OH, USA, in 2011 and 2015, respectively, all in electrical and computer engineering.

He was a Graduate Research Associate with the Electro-Science Laboratory, The Ohio State University, from 2008 to 2014. He was appointed as a Presidential Fellow with The Ohio State University in 2015, and is currently works with Intel Corporation, Santa Clara, CA, USA. His current research interests include multi-layered media analysis, particle-in-cell algorithms, finite-element methods, electrically small antennas, and computational lithography techniques in semiconductor industry.

Yuri A. Omelchenko received the Ph.D. degree in plasma physics from the Moscow Institute of Physics and Technology, Moscow, Russia, in 1991.

He did post-doctoral studies with the Space Research Institute, Moscow, from 1991 to 1993, and the Laboratory for Plasma Studies, Cornell University, Ithaca, NY, USA, from 1993 to 1998, where he developed his first computational particle-in-cell models and software in support of experiments involving magnetized plasmas with high-energetic ion beam components. He has made important contributions to the theory of energetic ion rings and field-reversed configurations. He has also developed algorithms based on event-driven multiscale asynchronous parallel simulation approach, enabling computational explorations of high-energy-density plasma systems that had been out of reach of conventional (time-stepping) models. His current research interests include simulations of inhomogeneous magnetoplasmas that are difficult to model with conventional particle and fluid codes due to severe computational constraints.

Fernando L. Teixeira (F'15) received the B.S. and M.S. degrees from the Pontifical Catholic University of Rio de Janeiro, Rio de Janeiro, Brazil, in 1991 and 1995, respectively, and the Ph.D. degree from the University of Illinois at Urbana–Champaign, Champaign, IL, USA, in 1999, all in electrical engineering.

He was a Post-Doctoral Associate with the Massachusetts Institute of Technology, Cambridge, MA, USA, from 1999 to 2000. He joined The Ohio State University, Columbus, OH, USA, in 2000, where he is currently a Professor with the Department of Electrical and Computer Engineering and also with the Electro-Science Laboratory. His current research interests include applied electromagnetics and computational physics.

Dr. Teixeira is a recipient of the Career Award from the National Science Foundation, the triennial Booker Fellowship from the International Union of Radio Science (USNC/URSI), and the Outstanding Young Engineer Award from the IEEE Microwave Society (MTT-S).. He served as the Chair of the Joint IEEE AP/MTT-S Columbus Chapter and was an Associate Editor and a Guest Editor of the IEEE ANTENNAS AND WIRELESS PROPAGATION LETTERS. He serves as an Associate Editor of *IET Microwaves, Antennas, and Propagation*.